Process parameters and surface treatment effects on the mechanical and corrosion resistance properties of Ti6Al4V components produced by laser powder bed fusion

Process parameters and surface treatment effects on the mechanical and corrosion resistance properties of Ti6Al4V components produced by laser powder bed fusion

- Gianluca Buffa,
- Dina Palmeri,
- Gaetano Pollara,
- Francesco Di Franco,
- Monica Santamaria &
- Livan Fratini

Abstract

Laser powder bed fusion is one of the additive manufacturing technologies which has developed more rapidly in recent years as it enables the production of very complex geometries. Titanium alloys are among the most popular materials in the aerospace industry thanks to excellent mechanical and corrosion resistance. The corrosion behavior and mechanical properties of samples made of Ti6Al4V and characterized by the geometrical features typical of brackets were investigated taking into account the effects of process parameters on porosity and microstructure. A comparison between the corrosion resistance of samples with complex geometry (3D) and specimens characterized by simple geometry (FLAT) was carried out to understand the role of the part geometry in the passive film formation mechanism, also highlighting the effect of the lack of passivation film formed naturally by exposure to air. Finally, the samples with complex geometry were anodized in a fluoride-free aqueous solution and the corrosion resistance was evaluated.

1 Introduction

The term Additive Manufacturing refers to a family of production technologies that allow the production of components with complex geometries, by a subsequent layering of material, starting from a digital 3D model [1]. Laser-based powder bed fusion of metals (PBF-LB/M) is one of the additive manufacturing technologies used for several industrial applications as it achieves the necessary objectives of parts accuracy and complexity [2]. The possibility of producing very complex geometries, simply by creating the appropriate Computer-aided Design (CAD) model, allows the production of lighter components for given mechanical properties, thus reducing the overall weight of the assembled product. In the aerospace industry, this translates into a final product that consumes less fuel, reducing both costs and the environmental impact due to gas emissions [3, 4]. Titanium alloys, magnesium alloy, and 316 L stainless steel are among the most popular metals used for industrial applications [5, 6].

Several studies related to the characterization of corrosion resistance products made of different materials using additive manufacturing technology are reported in the literature [7, 8]. In particular, Ti6Al4V alloys are widely used thanks to the excellent combinations of mechanical properties and corrosion behavior [9, 10].

As far as the corrosion resistance of titanium alloys is regarded, this is due to the spontaneous formation of a thermodynamic stable thin passive film (about 2–3 nm thick) on the surface as a consequence of the exposition to the oxidizing environment [11]. Qin et al. [12] showed how the passive film hinders the electrochemical dissolution of metals.

In the case of Ti6Al4V produced by additive manufacturing, the effect of microstructural characteristics and elemental segregation on the stability of the passive film is currently not clear yet. Seo and Lee [13] demonstrated that Additive Manufactured Ti6Al4V alloy with a higher α' phase distribution contained more defects, which are associated with higher donor density on the passive film observed using Mott–Schottky plots. These defects induce a higher susceptibility to pitting corrosion. The papers focusing on the influence of the surface finishing on the corrosion properties of Ti6Al4V produced by additive manufacturing are even more rare in the literature [14]. In 2015, De Damborenea

et al. [15] stated that additive-manufactured Ti6Al4V ELI scaffolds have lower corrosion resistance compared to flat samples in phosphate-buffered saline (PBS) solution at 37 °C as a result of the presence of defects inherent to the alloy processing and demonstrated that the corrosion resistance could be improved by anodizing. A high cooling rate along the building direction, associated with the PBF-LB/M process, favors metastable martensite α' formation in the microstructure of Ti6Al4V alloy in the as-fabricated state, resulting in the strengthening of material coupled to low ductility [16]. Usually, in order to improve the corrosion resistance of PBF-LB/M products, post-heat treatment is made to promote the decomposition of a fraction of α' phase into $\alpha + \beta$ phase. The formation of the β phase enhances the corrosion resistance of a material, as demonstrated by Dai et al. [17]. Due to the higher V content in the β phase, the oxide layer, which provides the corrosion resistance of the alloy, is more stable in the β phase than in the α' phase. A few papers report a connection between the degree of porosity of the material and the corrosion resistance of the same material [18, 19]. Moreover, Xie et al. [20] observed a coupled effect of porosity and of the percentage of β phase, which specifically showed that small pores together with the presence of β phase determine an increase in the corrosion resistance of the material.

Brackets are typical titanium alloy components widely used in the aerospace sector. These components, designed to hold two perpendicular parts together ensuring strength and integrity, offer a good opportunity to reduce costs, as mentioned above, using Additive Manufacturing [21]. In fact, due to their peculiar geometries, very high values of the so-called "buy-to-fly" ratio, denoting a significant waste of material, occur in the production of brackets by machining processes starting from blocks of titanium. It is worth noting that besides ensuring proper mechanical strength, aeronautical brackets must be characterized by excellent corrosion resistance, due to the extremely aggressive environment they are subjected to during their life cycle.

In this work, the corrosion behavior and mechanical properties of scaled reduction samples reproducing the geometrical features characterizing typical brackets, made of Ti6Al4V by PBF-LB/M, were investigated.

The decision to use a scale reduction of the complex geometry for the study was made to ensure the cost sustainability of the experimental campaign, still preserving the relationship between volumes, surfaces, and contours that

influence the active heat flows during the process. In addition, a comparison of the corrosion resistance characteristics of specimens with complex geometry (3D) with specimens characterized by simple geometry (FLAT) was carried out, after an initial surface polishing treatment, to investigate the effect of the geometry on the passive film formation mechanism. Then, the samples were anodized in a fluoride-free aqueous solution in order to induce the growth of a thin oxide barrier layer, and to evaluate the effect of this anodic film on their corrosion resistance. Different sets of process parameters, also resulting in an intensified intrinsic heat treatment of material and therefore promoting the decomposition of a fraction of α' phase into $\alpha + \beta$ phase, have been selected in order to explore the possibility to improve the corrosion resistance of as-fabricated PBF-LB/M material. Mechanical and microstructural properties such as Ultimate Tensile Strength (UTS), Elongation to failure (ETF), porosity, and β-phase content, if any, were measured for the AS samples for all selected process parameters in order to highlight the mechanical and defect characteristics of the samples that showed better corrosion resistance.

2 Materials and methods

2.1 Experimental procedure

Ti6Al4V powder supplied by SLM Solutions Group AG (Lübeck, Germany), with a mass density of 4.43 g/cm3 and size distribution of 20–63 μm (Fig. 1), was used in this study.

Fig. 1

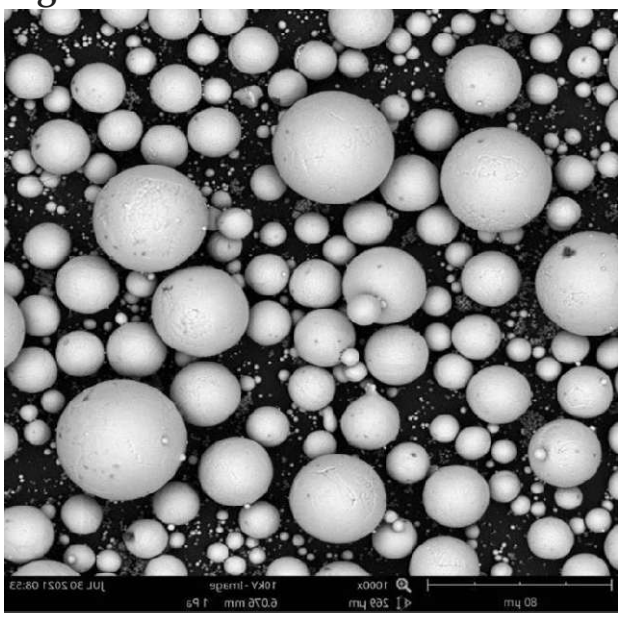

SEM image of Ti6Al4V spherical powder utilized

The experiments were carried out on an SLM 280HL machine. Two types of geometries were analyzed, a "3D sample" and a "flat sample", as shown in Fig. 2.

Fig. 2

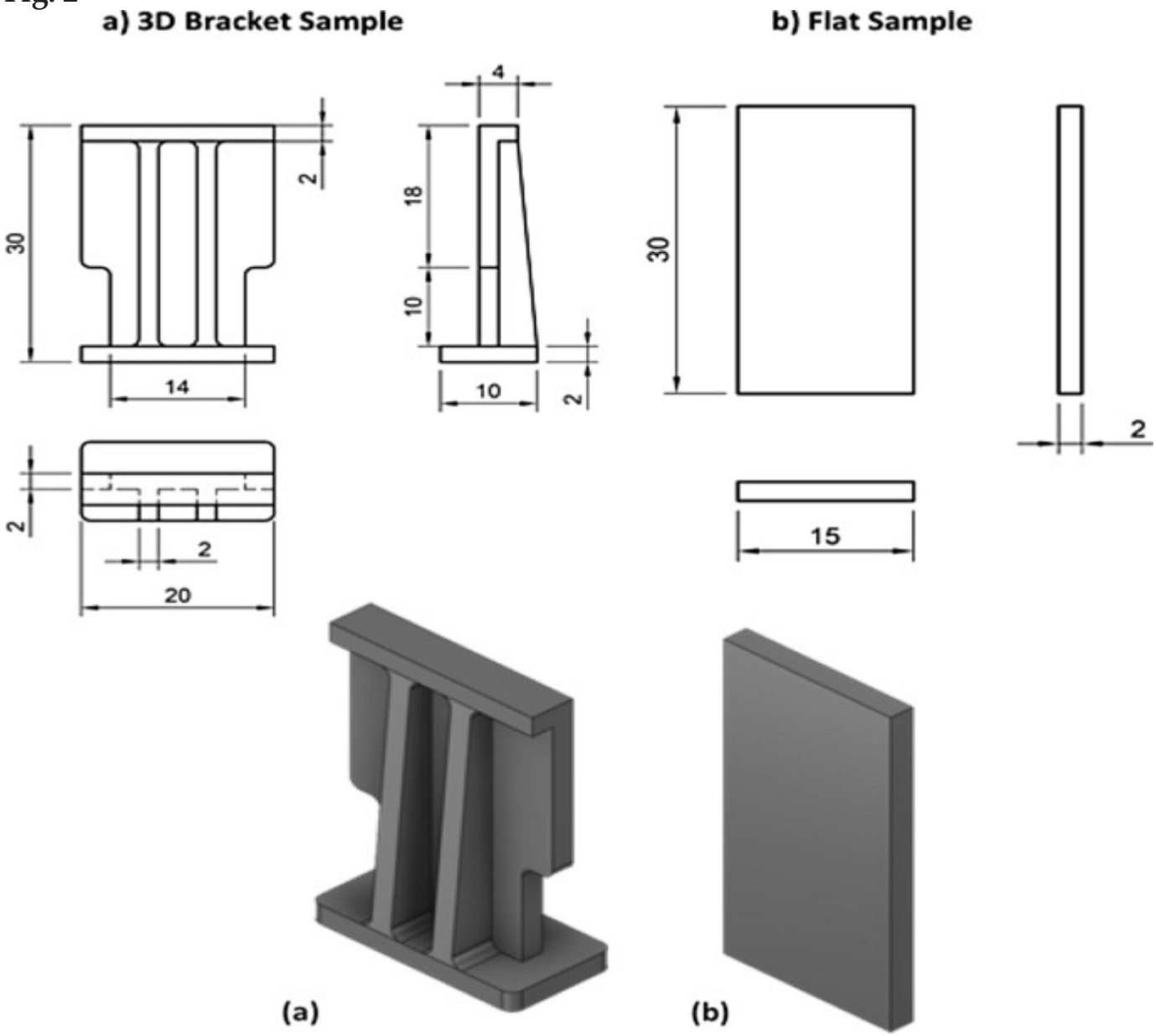

Samples geometries and dimensions in mm: **a** 3D sample, **b** Flat sample

Each sample was fabricated on a CP-Ti solid substrate preheated at 200 °C and the build chamber (280 × 280x365 mm) was filled with Argon to lower the Oxygen level to 0.1%.

For each geometry, nine different combinations of process parameters were used, as detailed in Table 1.

Table 1 Test ID and process parameters used

Test ID	P [W]	V [mm/s]	Scan strategy R [°]	LED [J/mm]	Layer Thickness [µm]	Hatch Distance [µm]	Build Orientation [°]
1	150	1400	15	0.11	30	120	45
2	150	1400	45	0.11	30	120	45
3	150	1400	90	0.11	30	120	45
4	350	1400	15	0.25	30	120	45
5	350	1400	45	0.25	30	120	45
6	350	1400	90	0.25	30	120	45
7	350	850	15	0.41	30	120	45
8	350	850	45	0.41	30	120	45
9	350	850	90	0.41	30	120	45

Three values of Line Energy Density (LED) (0.11 J/mm, 0.25 J/mm, 0.41 J/mm), with three different scan strategies, were investigated. The choice of the process parameters that determine the value of the Line Energy Density, i.e., laser power and scanning speed, was made taking into account two different factors that contribute to the increase of the corrosion resistance of the material: (i) the laser exposure time, a parameter proportional to the ratio between the sample volume and the scanning speed, whose increase favors the establishment of heat treatments intrinsic to the process which in turn, according to Barriobero-Vila et al. [22], promote the partial decomposition of the metastable phase α' into the two stable phases $\alpha + \beta$; (ii) the laser power, whose decrease results in lower values of residual stresses associated with the PBF-LB/M process and therefore better corrosion resistance characteristics of the material [23, 24].

The choice of the three LED levels was made, starting from values obtained by preliminary reference tests (LED 0.25 J/mm, $P = 350$ W, $V = 1400$ mm/s), in order to take into account the factors influencing the corrosion resistance. In particular, the LED value of 0.41 J/mm is related to an increase in the laser exposure time and takes into account the possibility of improving the corrosion resistance of the material due to the partial decomposition of the metastable phase α'. On the other hand, the LED value of 0.11 J/mm is related to a lower value of the laser power to which lower residual stress values are associated.

With reference to the scanning strategies used, they include a starting angle of 0°, a limiting scanning window of 180°, and an increasing scanning angle between consecutive layers of 15°, 45°, and 90° respectively. These three scanning strategies result in a periodicity of the number of layers, that is, the number of layers until the direction of the scan vector repeats in its initial direction, gradually decreasing. In fact, the periodicity associated with 15°, 45°, and 90° scan strategies is equal to 13, 5, and 3 layers, respectively. It is worth noting that

increasing values of the layer periodicity correspond to more homogeneous distributions of residual stresses intrinsically associated with the PBF-LB/M process [17, 25]. Layer thickness, hatch distance, and build orientation were kept constant to the values indicated in Table 1. The values of hatch distance and layer thickness have been chosen referring to the parameters recommended by SLM Solution. Finally, the choice of the building orientation, fixed at 45°, was made considering the configuration of the samples with a complex geometry that allowed to minimize the surfaces affected by the supports in the printing process (Fig. 3). This choice allowed to avoid the presence of superficial inhomogeneities correlated to the presence of the supports that could influence the evaluations about the resistance to corrosion of the samples.

Fig. 3

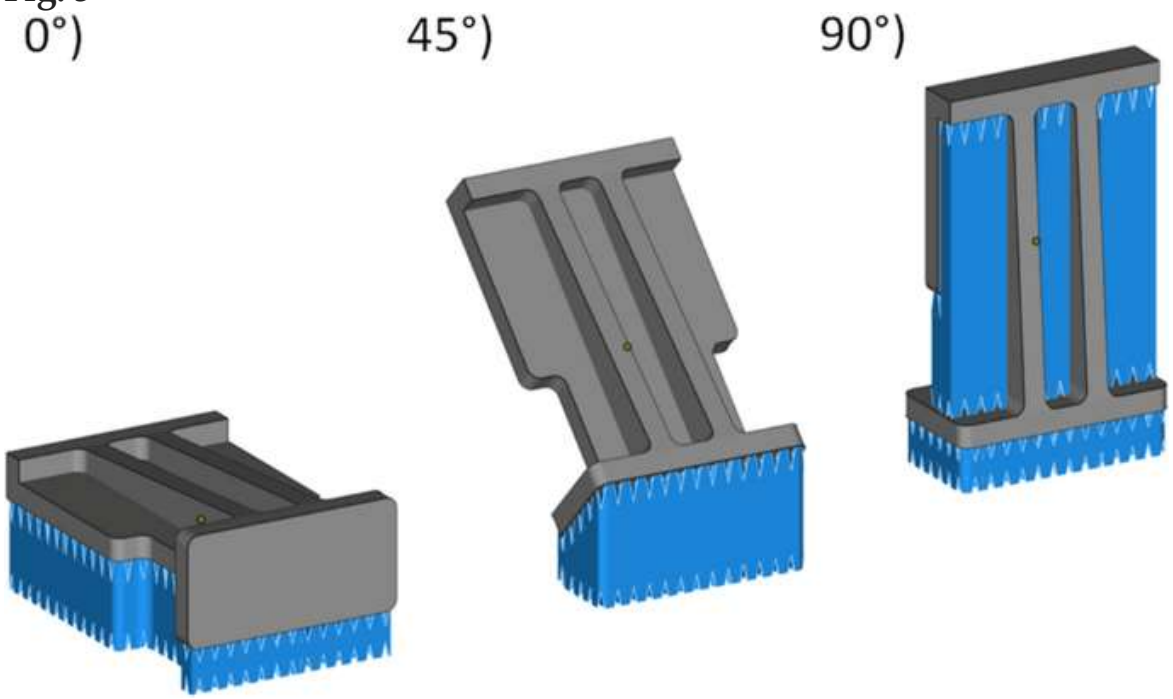

3D Samples support optimization for 45° building orientation

Three samples were fabricated for each set of process parameters and for each geometry. The three different repetitions of 3D and Flat specimens were used to perform microstructural analysis of the sample cross-sections, density measurements, and corrosion resistance analysis.

Additional dog-bone-shaped specimens were produced to carry out tensile tests. The three repetitions provided the average values of the mechanical properties of the material in terms of UTS and ETF, as shown in the next paragraph.

2.2 Mechanical, metallurgical, and corrosion tests

Density measurements were carried out on both 3D and Flat samples, using the Archimedes method at room temperature according to ASTM B96208, to assess the effectiveness of the considered process parameters. The samples were weighed in air (m_A) and in water (m_W) and the obtained values were used to calculate the relative density according to the following equation (Eq. 1):

$$\varrho = \frac{m_A}{m_A - m_W}\varrho_W \quad (1)$$

where ϱ_W is the density of water at room temperature.

A Mettler Toledo balance with an accuracy of ± 0.1 mg was used to measure the mass in air and in the fluid for each specimen. In order to estimate the relative density of the printed parts, the density of wrought Ti6Al4V equal to 4,43 g/cm^3 was used as a reference.

To evaluate the mechanical performance in terms of ultimate tensile strength and ductility (elongation to failure), a second set of samples with dog bone shape was designed as a reduction of Standard ASTM/E8 with a rectangular cross Sect. (15 × 2 mm) and a useful gauge length equal to 30 mm. The tensile tests were performed on a Galdabini universal testing machine.

The cross-section of the 3D and Flat samples was prepared for metallographic observations. After grinding and polishing, the specimens were etched with Kroll's reagent and observed through an Olympus Optical microscope in order to evaluate the microstructural modifications occurring as a function of the utilized process parameters. Scanning electron microscopy (SEM) analysis was carried out through Phenom ProX Desktop scanning electron microscope to highlight the powder morphology.

The crystalline structure of the specimens, before and after the growth of the anodic layer, was investigated by X-ray Diffraction (XRD), using CuKα radiation XRD patterns. X-ray diffractometer Pan Analytical Empyrean, equipped with a Cu anode (Kα radiation, λ = 0.15405 nm), was used.

The corrosion resistance of both 3D and flat samples was first assessed using 3.5% wt. NaCl solution at room temperature. Subsequently, with reference to 3D

geometries only, the samples were chemically etched (CE) in an acidic solution to remove the surface passive films grown by air exposure. Corrosion resistance characteristics were also measured for these samples to highlight the effect of the lack of passivation film formed naturally by exposure to air.

After this initial evaluation, the samples with complex geometry were anodized in a fluoride-free aqueous solution in order to induce the growth of a few nm thick barrier layer and to evaluate the effect of anodic films on their corrosion resistance. A two-electrode configuration was used, being the sample the working electrode and an Al 99.9% foil the counter electrode (cathode). The samples were drilled on the top and iron wires were connected in the holes for electrical connection before being sealed by paraffin.

Electrochemical characterization was carried out in 3.5 wt.% in NaCl aqueous solution to simulate seawater. After monitoring the Open Circuit Potential (OCP) for the 1800s, an Electrochemical Impedance Spectrum was recorded by superimposing to the OCP a 10 mV ac signal in the frequency range 100 kHz–100 mHz. Polarization curves were then recorded by scanning the electrode potential at 2 mV s^{-1} in 3.5 wt.% in NaCl solution using a Parstat 2263 potentiostat. All the electrochemical measurements were carried out with a three-electrode configuration cell. The tested sample was the working electrode, an Ag/AgCl/sat. KCl (0.197 V vs. Standard Hydrogen Electrode, SHE) was used as the reference electrode, and a Pt net with a high surface area as the counter electrode. Electrochemical measurements were carried out at least three times for all the samples. Impedance spectra were fitted with ZSimpWin software. Before the anodizing treatment, each 3D sample was chemically etched (CE) in a solution of 1:4:5 vol ratio of HF (40%): HNO_3 (68%): H_2O for 20 min at room temperature. Growth of the anodic layer was carried out in 0.1 M H_3PO_4 aqueous solution in order to produce a barrier-type anodic film. Anodizing was undertaken galvanostatically at 5 mA cm^{-2}, reaching the final voltage (i.e., formation voltage) of 40 V. Then, a stabilization process was carried out keeping the final voltage for 30 min. The mechanical polishing was carried out with a 2400 grit silicon carbide paper.

3 Results

3.1 Mechanical properties

The tensile test results are shown, in terms of both UTS and ETF average values, in Fig. 4. The trends obtained show better ductility for the samples produced with LED = 0.25 J/mm, while the best tensile strength values were found for the samples characterized by LED = 0.41 J/mm.

Fig. 4

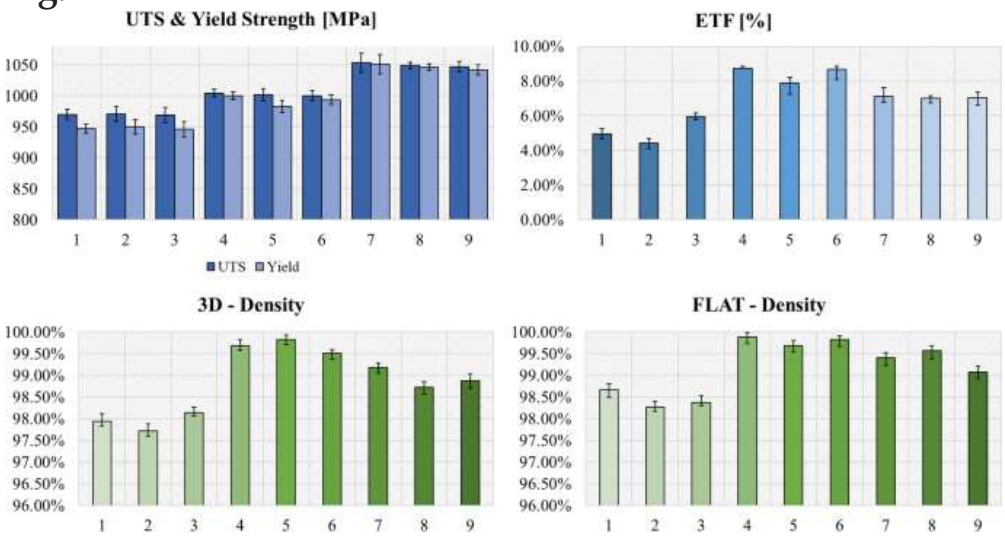

Mechanical characteristics (UTS, Yield Strength and ETF) for each set of process parameters and density for 3D and Flat samples

The obtained trends showed the prevailing effect of LED over scan strategy on UTS, ETF, and material density. In detail, only a little variation of UTS and ETF can be observed with varying scan strategies, while a more significant overall increment of the UTS can be noted by increasing the LED value. With regard to the ETF, a maximum can be reached by increasing the LED until 0.25 J/mm, while a higher value of LED determines a deterioration of the performance. Regarding the density values obtained for 3D complex geometry samples and simple flat geometry samples, the best values were found in the flat samples made with LED values of 0.25 J/mm with limited influence of the used scan strategy. A significant reduction in specimen density was found for specimens with an LED value of 0.11 J/mm with a more pronounced effect for the complex geometry specimens compared to the flat specimens.

3.2 Metallurgical and microstructural properties

Figures 5 and 6 show XRD patterns for Flat and 3D samples produced with varying process parameters. The produced samples are apparently dominated by α'/α -Ti phase, but a weak reflection at $2\theta = 39.7°$, relating to β-Ti phase, is present in both flat and 3D samples produced with high LED (0.41 J/mm) (see Figs. 5c and 6c), and in 3D samples produced with medium LED (0.25 J/mm) (see Fig. 6b).

Fig. 5

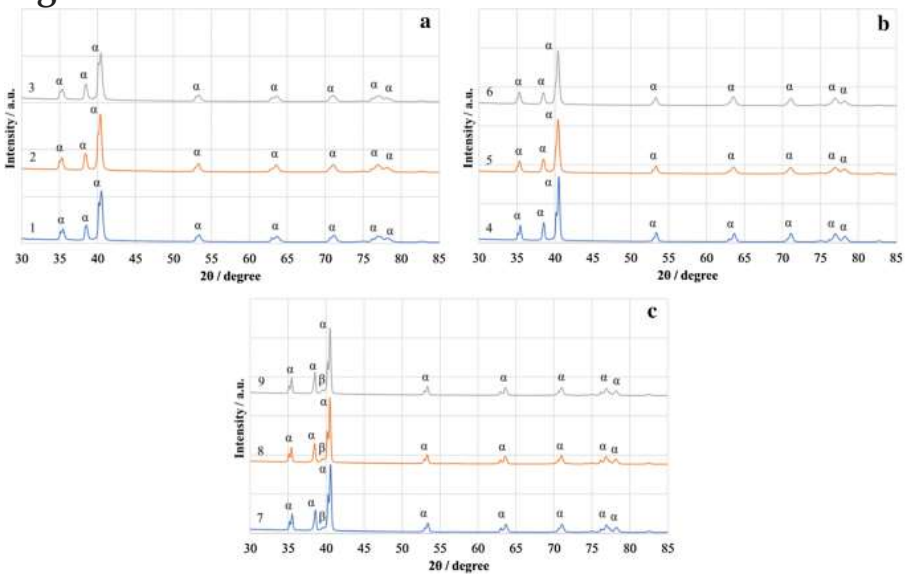

XRD patterns for Flat samples produced with different process parameters. The samples with the same LED were regrouped together. **a** Samples 1, 2, 3 with LED of 0.11 J/mm, **b** samples 4, 5, 6 with LED of 0.25 J/mm, **c** samples 7, 8, 9 with LED of 0.41 J/mm

Fig. 6

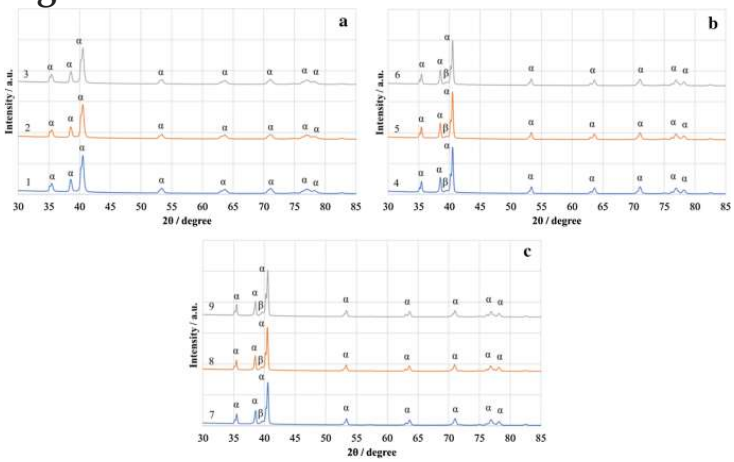

XRD patterns for 3D samples produced with different process parameters. The samples with the same LED were regrouped together. **a** Samples 1, 2, 3 with LED of 0.11 J/mm, **b** samples 4, 5, 6 with LED of 0.25 J/mm, **c** samples 7, 8, 9 with LED of 0.41 J/mm. It is worth noting that no significant difference in microstructure can be observed by varying scan strategy.

Usually, the Ti6Al4V alloy samples subjected to the LPBF process show a martensitic type microstructure, but in particular operating conditions, i.e., when the layer thickness and LED values are combined in such a way as to determine, in the execution of the different layers, an intensified intrinsic heat treatments of the material, the formation of phase $\alpha + \beta$ is enabled starting from phase α' which is formed in the first instance. In the cases examined, high LED values associated

with low layer thickness values (30 μm) contribute to determining the aforementioned conditions of thermal intensification. The different scanning strategies do not determine a variation in terms of the kind of phases present in the different samples for a given LED value, in agreement with the detected XRD trends; in fact, for fixed LED value, homogeneous trends of the XRD curves are observed when varying the scanning strategy. It is worth noting that these trends provide information about the phases present when the process parameters vary but do not give information about their specific distribution and content within the different samples. The microstructural analysis highlighted, for samples characterized by low LED values, the presence of diffuse and uniform porosity, due to a lack of fusion, within the cross-sections in both 3D and Flat samples (Fig. 7).

Fig. 7

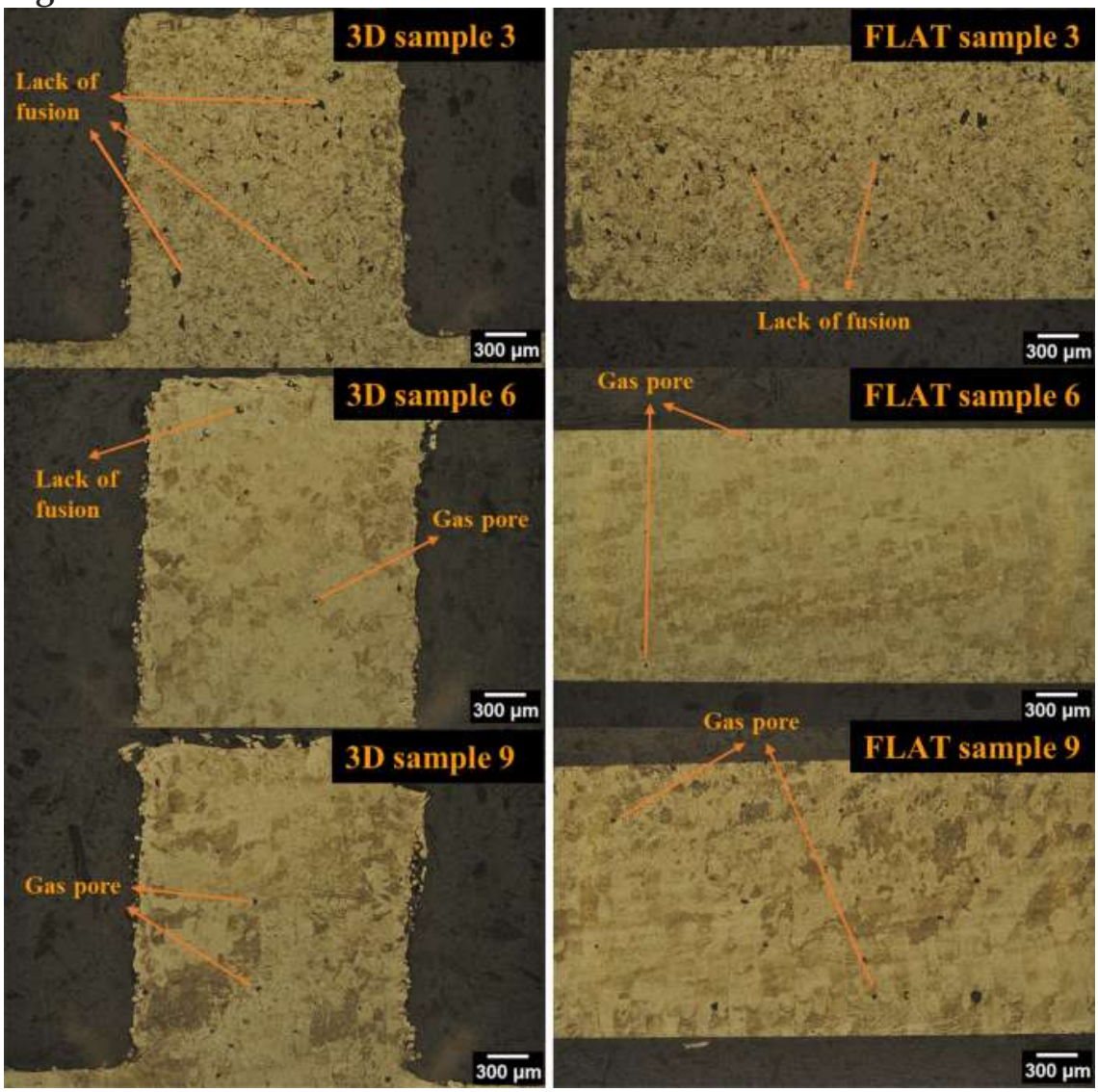

3D and flat samples microstructure

The microstructure of the samples was found to be martensitic with original grain morphology β within which the metastable martensitic phase of a non-equiaxial type developed. Intermediate LED values generated extremely reduced porosity, due to both gas pores and lack of fusion, with localized distribution near the edges of the samples and a homogeneous equiassic microstructure. Finally, high LED values resulted in small porosity defects, due to gas pores, with a homogeneous distribution in the cross-section of the samples. The observed microstructure for these samples is coarse equiassic α′ grains with small regions of α Widmanstätten structure surrounded by a small film of β phase [26], as highlighted in Fig. 8.

Fig. 8

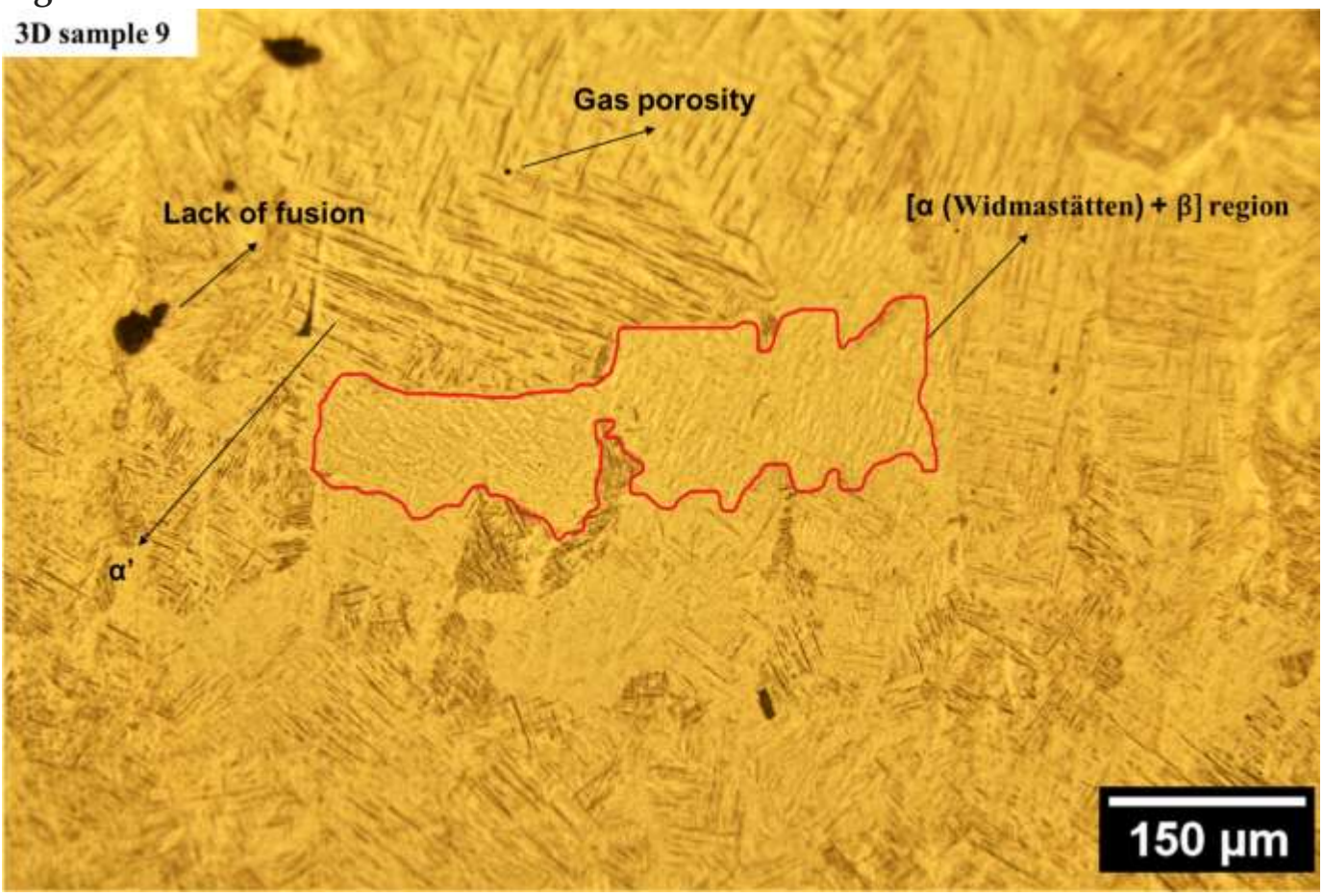

Microstructure of 3D sample 9 with large areas of α′ metastable martensite and small region of α + β phase. Lack of fusion and Gas porosity are also indicated

The aforementioned microstructural characteristics, in terms of the presence of porosity defects, were further supported by the outcome of the density measurements carried out and reported in Fig. 4. In particular, reduced density values were found in the specimens made with LED = 0.11 J/mm, both for 3D and FLAT specimens, although in the 3D specimens, the density reduction is more marked.

The best result, in terms of porosity, was obtained in the samples produced with LED = 0.25 J/mm, while, as mentioned, the high energy density of the samples produced with LED = 0.41 J/mm results in the formation of homogeneously distributed gas pore defects.

3.3 Corrosion properties

In order to evaluate the corrosion resistance of 3D and flat samples, electrochemical tests were carried out in an aggressive environment, i.e., a chlorides-rich electrolyte mimicking seawater. Figure 9 and Fig. 10 shows polarization curves for the as supplied (AS), i.e., as produced by PBF-LB/M, FLAT, and 3D samples after mechanical polishing for different LED values, as 0.11 J/mm, 0.25 J/mm, 0.41 J/mm, as the scanning strategy changes.

Fig. 9

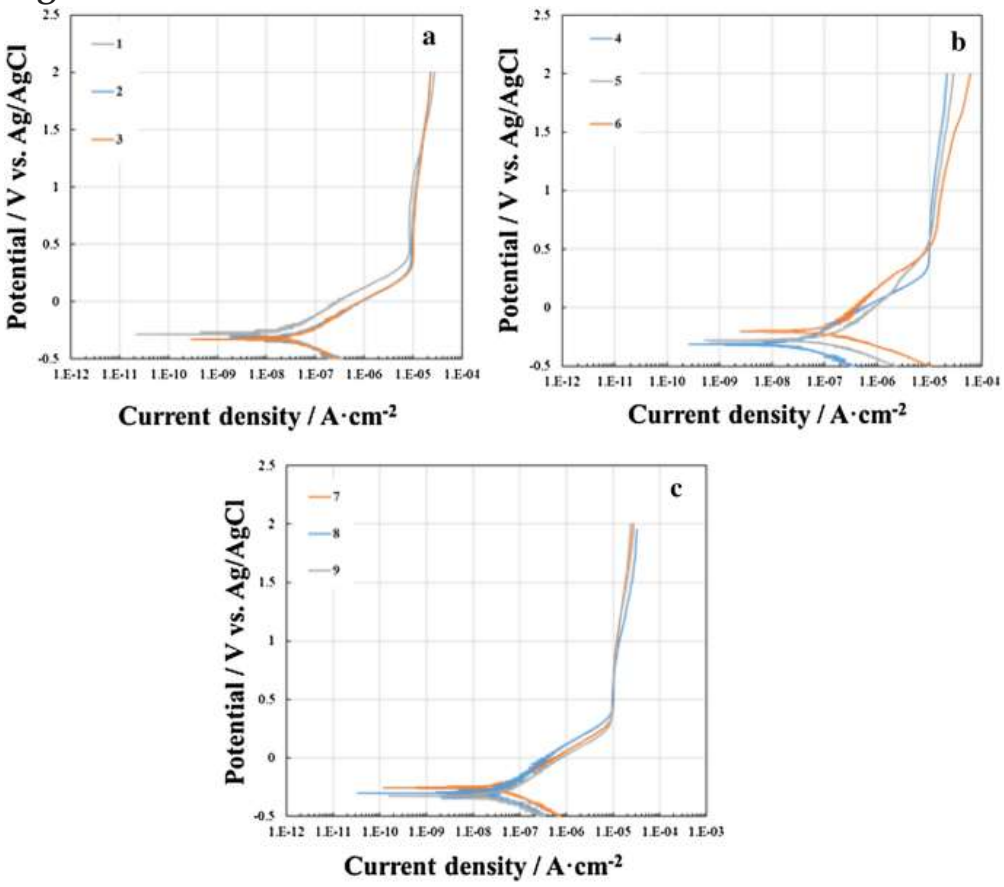

Potentiodynamic Polarization curves for AS Flat samples after mechanical polishing for different LED values. **a** 0.11 J/mm, **b** 0.25 J/mm, **c** 0.41 J/mm

Fig. 10

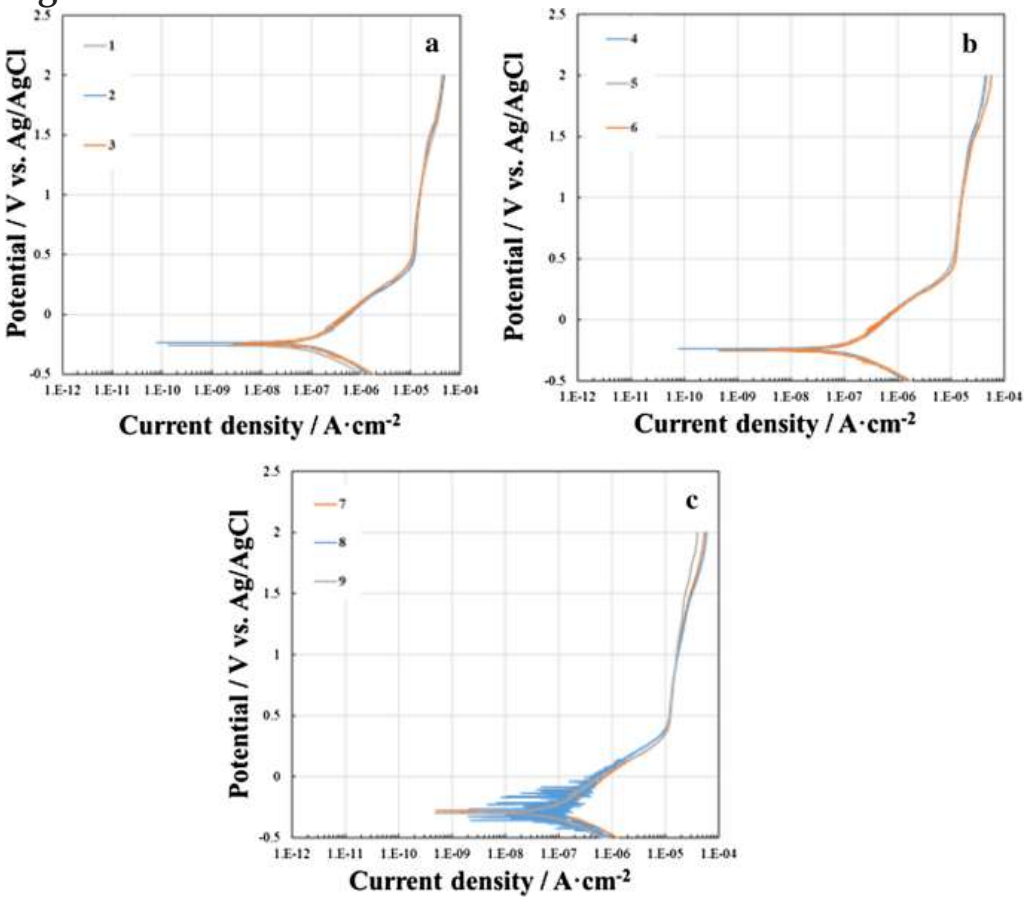

Potentiodynamic Polarization curves for AS 3D samples after mechanical polishing for different LED values. **a** 0.11 J/mm, **b** 0.25 J/mm, **c** 0.41 J/mm

The corresponding values of the corrosion parameters deduced from the above-mentioned polarization curves are instead given in Table 2, for the flat samples, and in Table 3 for the 3D samples. The E_{corr} (corrosion potential) and i_{corr} (corrosion current density) parameters estimated using the Tafel extrapolation method and the i_{pass} (passivity current density) parameter at 2 V vs. Ag/AgCl are summarized.

Table 2 Corrosion parameters for AS FLAT samples mechanically polished with LED of 0.11 J/mm, 0.25 J/m, 0.41 J/mm and for the different scan strategies

LED	Test ID	Surface Treatment	E_{corr} [V] vs. Ag/AgCl	i_{corr} [A/cm^2]	i_{pass} [A/cm^2]
0.11 [J/mm]	1	AS	− 0.26	$2.0\,10^{-8}$	$2.7\,10^{-5}$
	2	AS	− 0.29	$3.5\,10^{-8}$	$2.3\,10^{-5}$
	3	AS	− 0.31	$3.0\,10^{-8}$	$2.3\,10^{-5}$
0.25 [J/mm]	4	AS	− 0.30	$2.0\,10^{-8}$	$2.1\,10^{-5}$
	5	AS	− 0.29	$1.3\,10^{-7}$	$2.9\,10^{-5}$
	6	AS	− 0.21	$1.2\,10^{-7}$	$5.8\,10^{-5}$
0.41 [J/mm]	7	AS	− 0.24	$3.5\,10^{-8}$	$2.7\,10^{-5}$
	8	AS	− 0.30	$3.0\,10^{-8}$	$3.1\,10^{-5}$
	9	AS	− 0.31	$3.7\,10^{-8}$	$2.4\,10^{-5}$

Table 3 Corrosion parameters for AS 3D sample mechanically polished with LED of 0.11 J/mm, 0.25 J/m, 0.41 J/mm and for the different scan strategies

LED	Test ID	Surface Treatment	E_{corr} [V] vs. Ag/AgCl	i_{corr} [A/cm^2]	i_{pass} [A/cm^2]
0.11 [J/mm]	1	AS	- 0.27	$7.0\,10^{-8}$	$4.7\,10^{-5}$
	2	AS	- 0.23	$1.2\,10^{-7}$	$4.6\,10^{-5}$
	3	AS	- 0.23	$1.0\,10^{-7}$	$4.3\,10^{-5}$
0.25 [J/mm]	4	AS	- 0.24	$1.0\,10^{-7}$	$4.6\,10^{-5}$
	5	AS	- 0.23	$1.3\,10^{-7}$	$4.3\,10^{-5}$
	6	AS	- 0.23	$1.0\,10^{-7}$	$5.7\,10^{-5}$
0.41 [J/mm]	7	AS	- 0.29	$1.3\,10^{-7}$	$5.3\,10^{-5}$
	8	AS	- 0.26	$7.0\,10^{-8}$	$5.9\,10^{-5}$
	9	AS	- 0.29	$6.7\,10^{-8}$	$3.9\,10^{-5}$

Figure 11 shows the polarization curves for the AS, chemically etched (CE), and anodized (AN) samples for different LED values and scan strategies. In Table 4 E_{corr} and i_{corr}, estimated using the Tafel extrapolation method and the i_{pass} at 2 V vs. Ag/AgCl, deduced from polarization curves, are summarized.

Fig. 11

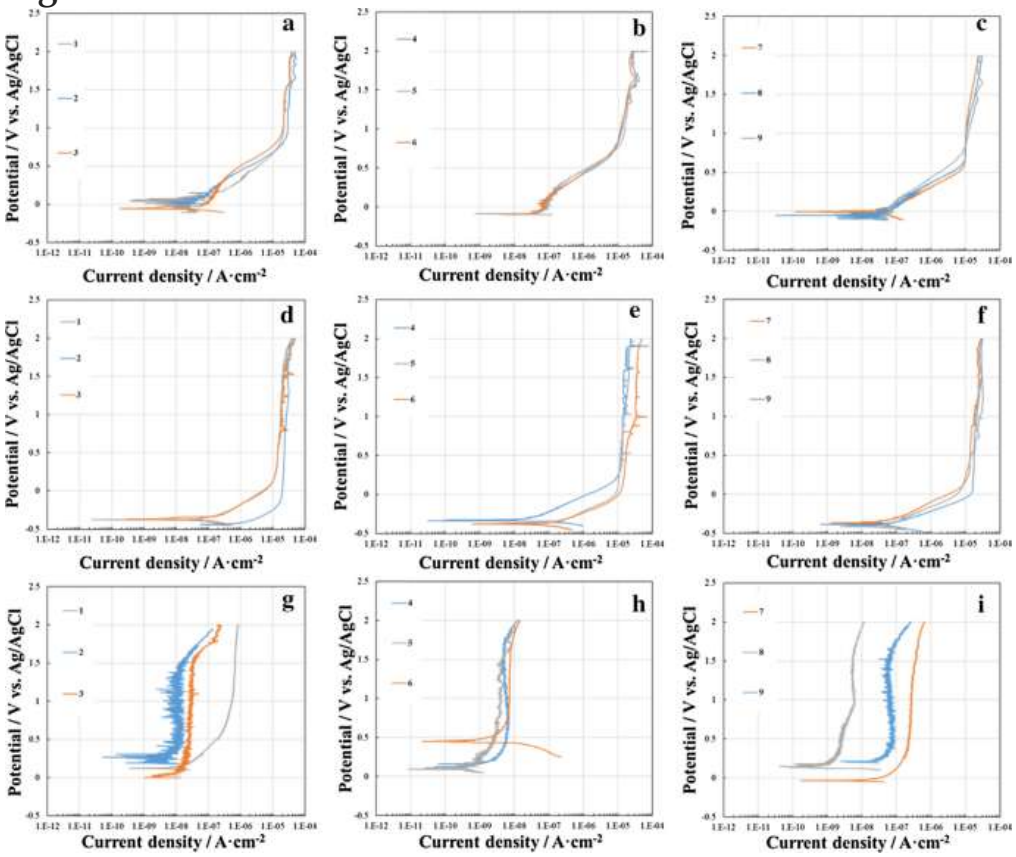

Potentiodynamic Polarization curves for 3D samples: as supplied (AS) (**a, b, c**), chemically etched (CE) (**d, e, f**) and anodized (AN) (**g, h, i**). Samples for different LED values a, d, g, LED = 0.11 J/mm, b, e, h LED = 0.25 J/mm, c, f, i LED = 0.41 J/mm

Table 4 Corrosion parameters for 3D sample

LED	Test ID	Surface Treatment	E_{corr} [V] vs. Ag/AgCl	i_{corr} [A/cm^2]	i_{pass} [A/cm^2]
a) 0.11 [J/mm]	1	AS	0.02	$1.4\,10^{-8}$	$4.2\,10^{-5}$
	2	AS	0.02	$3.9\,10^{-8}$	$4.8\,10^{-5}$
	3	AS	- 0.08	$8.1\,10^{-8}$	$3.9\,10^{-5}$
	1	CE	- 0.35	$1.3\,10^{-7}$	$4.4\,10^{-5}$
	2	CE	- 0.41	$5.2\,10^{-7}$	$4.5\,10^{-5}$
	3	CE	- 0.35	$1.3\,10^{-7}$	$4.5\,10^{-5}$
	1	AN	0.10	$1.8\,10^{-8}$	$8.7\,10^{-7}$
	2	AN	0.26	$3.9\,10^{-8}$	$1.1\,10^{-7}$
	3	AN	0.02	$1.0\,10^{-9}$	$2.5\,10^{-7}$
b) 0.25 [J/mm]	4	AS	- 0.08	$3.9\,10^{-8}$	$2.5\,10^{-5}$
	5	AS	- 0.08	$3.9\,10^{-8}$	$2.5\,10^{-5}$
	6	AS	- 0.08	$3.9\,10^{-8}$	$2.5\,10^{-5}$
	4	CE	- 0.32	$4.3\,10^{-8}$	$2.4\,10^{-5}$
	5	CE	- 0.39	$1.0\,10^{-7}$	$2.4\,10^{-5}$
	6	CE	- 0.39	$1.0\,10^{-7}$	$4.9\,10^{-5}$
	4	AN	0.16	$2.0\,10^{-10}$	$1.2\,10^{-8}$
	5	AN	0.08	$4.0\,10^{-10}$	$1.2\,10^{-8}$
	6	AN	0.44	$6.4\,10^{-10}$	$1.3\,10^{-8}$
c) 0.41 [J/mm]	7	AS	0.01	$2.6\,10^{-8}$	$2.3\,10^{-5}$
	8	AS	- 0.09	$2.3\,10^{-8}$	$3.0\,10^{-5}$
	9	AS	- 0.09	$2.3\,10^{-8}$	$2.3\,10^{-5}$
	7	CE	- 0.39	$4.0\,10^{-8}$	$3.1\,10^{-5}$
	8	CE	- 0.42	$4.0\,10^{-8}$	$3.1\,10^{-5}$
	9	CE	- 0.40	$6.7\,10^{-8}$	$3.1\,10^{-5}$
	7	AN	- 0.05	$4.4\,10^{-8}$	$6.4\,10^{-7}$
	8	AN	0.12	$8.0\,10^{-10}$	$1.1\,10^{-8}$
	9	AN	0.22	$2.5\,10^{-8}$	$2.7\,10^{-7}$

The corrosion parameters obtained from the polarization curves, such as the corrosion potential E_{corr}, the corrosion current density i_{corr}, and the passivation current density i_{pass}, provide a plurality of information regarding the corrosion resistance characteristics of the material. In particular, corrosion potential is a mixed potential (also an open-circuit potential) at which the rate of anodic oxidation of the electrode equals the rate of cathodic reactions and there is no net current flowing in or out of the electrode. Corrosion current density is the current density at the corrosion potential and this is related to the rate at which the corrosion reaction occurs.

The passivation current density is related to the kinetics of the passivation reaction typical of titanium alloys which tend to be covered by a passivation film.

In the mechanically polished flat samples (AS), E_{corr} is more cathodic when the scan strategy used promotes less homogenization of residual stresses generated by the additive process due to a lower number of the periodic repetition of layers, in the case of samples made with LED values of 0.11 and 0.41 J/mm.

It should be noted that the surface mechanical polishing phase does not significantly affect the residual stress values associated with the LPBF process as these values are distributed within the entire volume of material and not only on the surface. Besides, the thickness of the material removed by mechanical polishing is about 60 μm which is assumed neglectable as compared to the sample thickness (2 mm).

For intermediate values of LED, i.e., 0.25 J/mm, instead, an opposite trend is observed, with the corrosion potential E_{corr} that increases in the case of samples made with scanning strategies that result in greater homogeneity between layers. However, as the homogeneity between the layers decreases, a significant decrease in the corrosion resistance of the material is observed for samples made with LED of 0.25 J/mm; in fact, the i_{corr} parameter takes on increasing values. In the 3D samples mechanically polished, the onset of corrosion phenomenon is marginally affected by the used scanning strategy; in fact, the E_{corr} assumes nearly constant values. On the other hand, regarding the corrosion resistance characteristics, which increase as the i_{corr} parameter decreases, a significant decrease in corrosion resistance is observed for samples made with 0.11 J/mm LEDs, with a lower degree of homogeneity between the different layers, from ~ 10^{-8} to ~10^{-7} A/cm^2. For the samples made with LED 0.25 J/mm, the corrosion resistance is limited to ~ 10^{-7} A/cm^2, while, for the samples made with LED equal to 0.41 J/mm there is an increase in corrosion resistance that goes from the value ~ 10^{-7} A/cm^2 for sample 7, which has more homogeneity between the layers, to the value ~ 10^{-8} A/cm^2 for the scanning strategies that determine less homogeneous layers.

For all samples, both 3D and Flat, the value of the i_{pass} parameter, is ~ 10^{-5} A/cm^2, and denotes good passivation kinetics of the material.

The comparison of the corrosion parameters for 3D AS mechanically polished samples and 3D AS samples shows an improvement in the corrosion resistance characteristics of the material for all the considered LED values and also for all

the scanning strategies. Table 4 shows that the i_{corr} parameter for 3D AS samples is equal to ~ 10^{-8} A/cm^2 for all scanning strategies and LED values considered.

For the AS-supplied 3D samples independently of the manufacturing parameters, E_{corr} is ~ 0 V vs. Ag/AgCl and passivity current density is ~ 10^{-5} A/cm^2. These values confirm the good corrosion performance of AS material and result close to those reported in the literature for Ti6Al4V ELI grade samples produced by additive manufacturing [24] and Ti6Al4V ELI casting samples [27].

At a potential of ~ 1.6 V vs. Ag/AgCl, all polarization curves show the presence of a current peak due to the dissolution of vanadium oxide in the passive film as vanadate ions, in agreement with Pourbaix Diagram [28]. Before the anodizing process, the samples were chemically etched (CE) in acidic solution to remove from the surface passive films grown by air exposure. Polarization curves recorded soon after this treatment show that the corrosion potential for all samples becomes is significantly more negative (i.e., − 0.5 V vs. Ag/AgCl), and the passive current density significantly higher without a marked onset of transpassivity. Indeed, in the case of CE samples polarization curves do not show any current peak at 1.6 V vs. Ag/AgCl, indicating that chemical etching completely removes vanadium oxide from the surface. As reported in Table 4, the passivity current for as-supplied and chemically etched samples is in the order of ~ 10^{-5} A cm^{-2}, close to the passivity current values reported in the literature for Ti6Al4V ELI grade samples produce by additive manufacturing [24] and Ti6Al4V ELI casting samples [27].

In the CE samples, a significant reduction in the corrosion resistance of the material is observed for all scan strategy values and for LED values of 0.11 J/mm and in the case of LED values of 0.25 J/mm for scan strategy values that promote inhomogeneity between layers (samples 5 and 6). For the samples obtained with LED values of 0.41 J/mm, no significant variations in corrosion resistance parameters are observed between the AS and CE samples.

All the AN sample show better corrosion characteristics with respect to the AS and CE samples in fact the i_{corr} takes on values of the order of ~ 10^{-9}, 10^{-10} A/cm^2.

In Fig. 12 the voltage vs time curve recorded during the anodizing process is reported. According to the high field mechanism [28] a constant slope, $_{dV/dt}$, is expected (Eq. 2):

$$dVdt=\eta jEdMzF\varrho$$

(2)

in which j is the current density (kept constant in this case during the anodizing process), M is the molecular weight of the growing oxide, z is the number of electrons circulating per mole of formed oxide, F is the Faraday constant, ρ is the film density and E_d is the electric field strength across the growing layer, and η is the growth efficiency.

Fig. 12

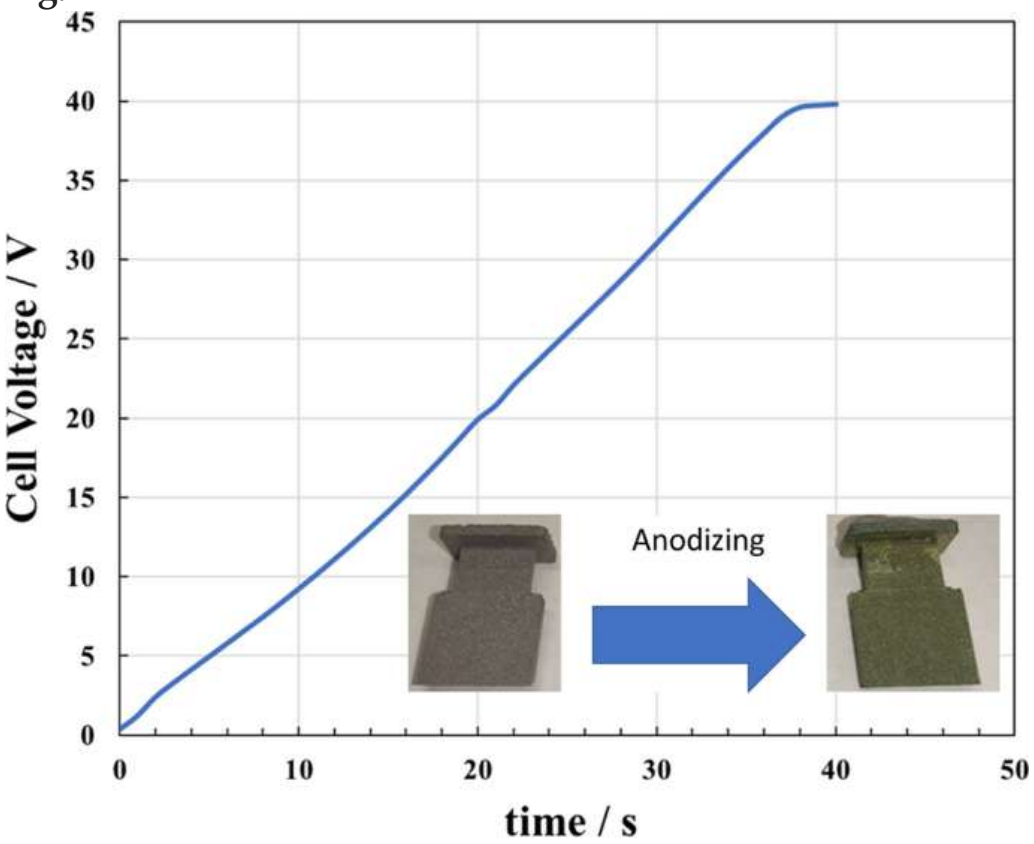

Voltage vs time curve recorded during the anodizing process

It is important to mention that a constant $_{dV/dt}$ suggests that no breakdown phenomena occur during film growth. In this way, a growth efficiency close to 1 (Eq. 2), $\rho = 3.7$ g cm^{-3} [29], $E_d = 3.6$ MV cm^{-1} can be estimated, corresponding to an anodizing ratio (i.e., the reciprocal of the electric field strength) of ~ 25 Å V^{-1}.

Thus, assuming an equilibrium potential for Ti oxidation to TiO_2 of ~—1.2 V (SHE) [30], formation voltages of 40 V (vs. cathode) correspond to an anodic layer thickness of ~ 100 nm. After the anodizing process, the samples' surfaces appear blue/green colored due to the oxide optical interference (see inset Fig. 12). After the anodizing treatment, all the samples were characterized by recording the polarization curves in NaCl solution. By comparing the corrosion parameters extrapolated from the polarization curves relating to the AN samples with those estimated for the other samples (see Table 4), it is possible to note an enhancement in the corrosion resistance of the Ti alloy samples after the anodizing process. EIS spectra were recorded to have a further understanding on the influence of the processing route and surface treatments on the corrosion behavior. Figure 13 shows EIS spectra recorded for all samples in the Bode plot representation.

Fig. 13

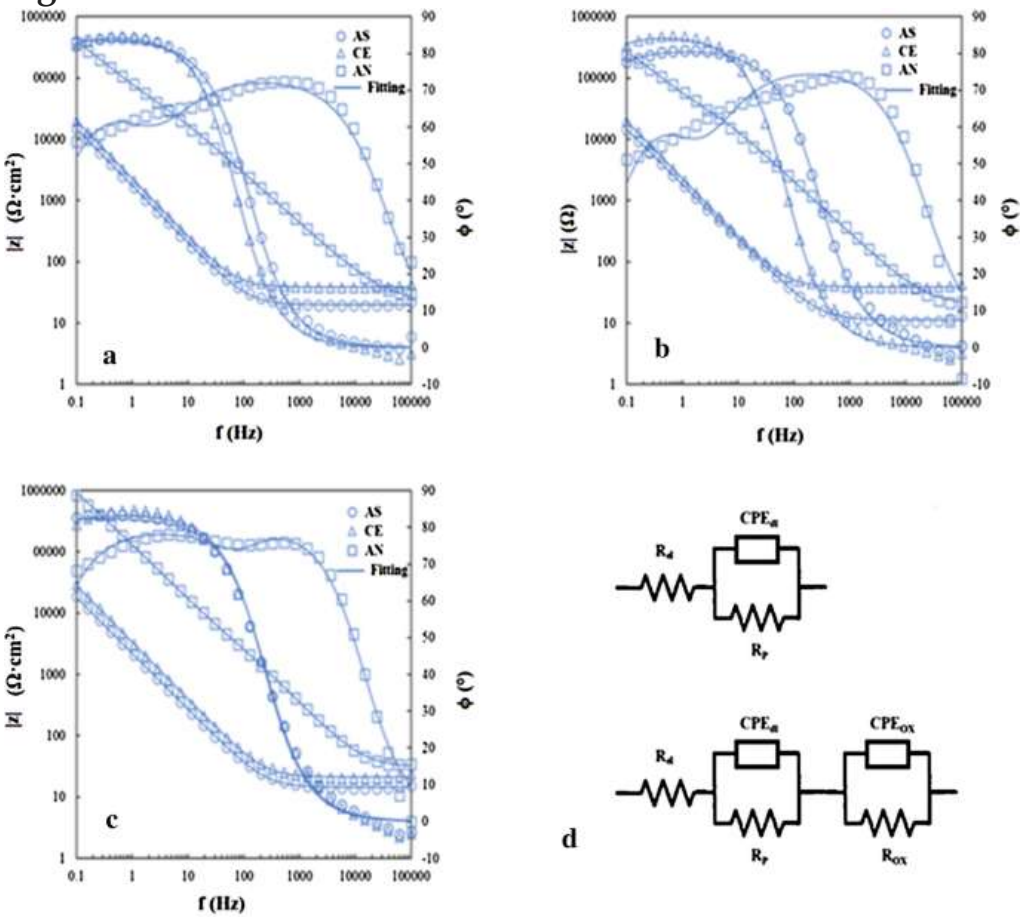

EIS spectra in Bode representation recorded during immersion in 3.5% wt. NaCl solution at the corresponding corrosion potential for as supplied (AS), chemically etched (CE) and anodized (AN) 3D samples and for different LED parameters. Samples with the same LED value were represented by the intermediate EIS spectrum as the scanning strategy changed. **a** Samples with LED of

0.11 J/mm, **b** samples with LED of 0.25 J/mm, **c** samples with LED of 0.41 J/mm. **d** Electric equivalent circuits to model EIS spectra for AS and CE samples (top) and AN samples (bottom)

In the case of AS and CE samples, the EIS spectra show the presence of only one time constant while in the case of anodized samples two time constants appear. This could be explained by considering the presence of anodic oxide on the metal surface. However, it cannot be excluded that the two time constants are related to the presence of crystalline regions associated with the crystallization of the film during anodizing. [31]. According to this behavior, the EIS spectra can be modeled according to the equivalent circuits reported in Fig. 13d. In the case of as supplied and chemically etched samples, the equivalent circuit is composed of a resistance element, R_{el}, that represents the resistance of the electrolyte, that is in series with a parallel between a Constant Phase Element CPE_{dl} and polarization resistance R_P. CPE_{dl} is a constant phase element introduced to model the not ideal capacitance of the metal/electrolyte interface and takes into account the inhomogeneity present at the solid/liquid interface. Polarization resistance takes into account the kinetic of both anodic and cathodic processes during the corrosion processes due to the immersion in NaCl solution. In the case of the anodized samples, to consider the presence of the anodic oxide, a second parallel between a Constant Phase Element CPE_{ox} (to model the not ideal oxide capacitance) and oxide resistance R_{ox} is added. In Table 5 the corresponding fitting parameters are reported. Polarization resistance values for as supplied and anodized samples, for LED values of 0.11 and 0.25 J/mm, are in the order of ~ 10^6 Ω·cm², suggesting the formation of a good protective passive film on the surface, in agreement with the results of polarization curves.

Table 5 EIS fitting parameters

Sample	Surface Treatment	R_{el} [Ω cm²]	R_p [Ω cm²]	CPE_{dl} [S s^n cm^{-2}]	n_{dl}	R_{ox} [Ω cm²]	CPE_{ox} [S s^n cm^{-2}]	n_{ox}
a)	AS	18 ± 4	$(1.0 \pm 0.1) \cdot 10^6$	$(7.5 \pm 1)\,10^{-5}$	0.92 ± 0.01	/	/	/
	CE	40 ± 20	$(6.0 \pm 4)\,10^5$	$(4.5 \pm 1)\,10^{-5}$	0.93 ± 0.01	/	/	/
	AN	28 ± 2	$(3.0 \pm 2)\,10^6$	$(3.5 \pm 2)\,10^{-6}$	0.84 ± 0.03	$(1.3 \pm 0.3) \cdot 10^4$	$(1.6 \pm 0.2)\,10^{-5}$	0.84 ± 0.03
b)	AS	30 ± 10	$(1.0 \pm 0.1)\,10^6$	$(8.0 \pm 2)\,10^{-5}$	0.92 ± 0.01	/	/	/
	CE	40 ± 20	$(6.5 \pm 5)\,10^5$	$(5.5 \pm 1)\,10^{-5}$	0.93 ± 0.01	/	/	/
	AN	25 ± 5	$(1.3 \pm 0.3) \cdot 10^6$	$(4.3 \pm 1)\,10^{-6}$	0.82 ± 0.01	$(3.5 \pm 1.5) \cdot 10^4$	$(6.0 \pm 2) \cdot 10^{-6}$	0.84 ± 0.02
c)	AS	11 ± 4	$(2.2 \pm 0.1) \cdot 10^5$	$(8.0 \pm 2)\,10^{-5}$	0.92 ± 0.01	/	/	/
	CE	40 ± 20	$(8.0 \pm 5)\,10^5$	$(5.5 \pm 2)\,10^{-5}$	0.93 ± 0.01	/	/	/
	AN	25 ± 5	$(8.0 \pm 3) \cdot 10^5$	$(5.0 \pm 3) \cdot 10^{-6}$	0.85 ± 0.01	$(2.5 \pm 1)\,10^4$	$(3.4 \pm 0.4)\,10^{-6}$	0.85 ± 0.01

Lower values of polarization resistance, ~ 10^5 Ω·cm^2, were found for the CE samples with LED equal to 0.11 and 0.25 J/cm and for the samples with LED 0.41 independently of the AS, CE, or AN condition. In the case of anodized samples, the formation of a blocking anodic oxide (oxide resistance in the order of ~ 10^4 Ω·cm^2) significantly improves their corrosion performance, regardless of the LED used during the PBF-LB/M process.

4 Discussion

The corrosion resistance of the samples was evaluated taking into account the used process parameters. The mechanical and microstructural properties such as UTS, ETF, porosity, and the possible content of β-phase were measured for the AS samples. For the flat samples, the most influential factors on the corrosion resistance of the material are the degree of homogenization of the layers and the porosity distribution; in fact, the best corrosion resistance values were observed for samples 1, 4, and 7. However, it was observed that low material density values result in poor mechanical properties, UTS, and ETF (see for instance specimen 1). As the LED increases (0.25 J/mm) larger density values were measured and, as a consequence, better mechanical properties were observed. On the other hand, the samples characterized by LED equal to 0.25 J/mm showed significantly decreasing corrosion resistance values as the degree of homogenization between the layers decreases. The significant reduction in the i_{corr} parameter can be attributed to the peculiar distribution of porosity observed. For these samples, the defect distribution is more localized near the edges of the samples. The mechanical treatment exposes the defect more to the corrosive environment and therefore the samples with the lowest corrosion resistance characteristics are samples 5 and 6. The particular geometric arrangement of the defects resulting from the process parameters above described, together with scan strategy values which determine non-homogeneous distributions of the residual stresses associated with the LPBF process in the production of each single layer, determines an increased susceptibility of the material to corrosive processes. It should also be noted that as the scan strategy angle increases, the number of layers which by subsequent overlapping restores the original deposition orientation decreases and therefore the number of layers in which the residual stresses associated with the process are reoriented and redistributed decreases.

For the mechanically polished 3D samples, it can be observed that in the samples made with 0.11 J/mm LED a homogeneous distribution of the layers favors an increase in corrosion resistance, while in the samples made with 0.25 J/mm LED

the effect of the perimeter distribution of the porosity defects prevails, leading to low corrosion resistance values. This effect is greater than the one observed in the case of the flat samples because the complex geometry leads to a greater surface extension of the sample for a given volume. In the samples made with LED equal to 0.41 J/mm, a further influential factor prevails in the improvement of the material corrosion resistance. In this case, the formation of a predominantly metastable martensitic α' microstructure is favored contributing, together with small percentages of $\alpha + \beta$ biphasic microstructure, to the improvement of the material corrosion resistance. It should also be noted that for the aforementioned samples, the operating conditions that promote homogeneity between the layers also lead to an intensification of the perimeter porosity defect. Such defect produces a decrease in the value of $i_{corr} \sim 10^{-7}$ A/cm^2, as observed for sample 7. For the 3D AS sample not undergoing mechanical polishing, improved corrosion resistance was observed because of the absence of the detrimental effects given by the removal of the natural passivation layer of the AS specimens with an exposure of the perimeter porosity defect. The trends of the i_{corr} for the CE samples show that the removal of the passivation layer of the samples produces, in general, a worsening of the corrosion resistance characteristics of the material. However, for the samples made with LED 0.41 J/mm, this effect is overridden by the positive one produced by the presence of β phase, explaining why the corrosion resistance characteristics of the CE samples remain almost unchanged compared to the AS samples. The best corrosion resistance values for AN samples were obtained for samples made with 0.25 J/mm and 0.41 J/mm LEDs, highlighting the positive effect produced by the presence of β phase. Finally, it is observed that the EIS results for the AN samples are in agreement with the results of polarization curves.

5 Summary and conclusions

In the paper, the results of an experimental study on the corrosion resistance of complex parts, typical of aeronautical applications, produced by PBF-LB/M are presented. Nine different process conditions, obtained with varying PBF-LB/M process parameters, were investigated on both 3D and flat samples. The corrosion resistance was then evaluated for as supplied and mechanically polished, as supplied, chemically etched, and anodized components. The corrosion resistance performance of the specimens produced under varying process parameters was evaluated taking into account the main factors influencing the corrosion resistance of the material.

From the obtained results, the following main conclusions can be drawn:

- The measurement of mechanical performances of AS samples highlighted that the effect of LED prevails over the one of scan strategy when UTS, ETF, and material density are considered. Limited variability of UTS and ETF with scan strategy was observed, while a significant increment of the UTS can be noted by increasing the LED value. As regards the ETF, a maximum can be reached by increasing the LED until 0.25 J/mm, while a higher value of LED determines a detrimental effect. The ETF and density show consistent trends.

- The microstructure of the AS samples made with LED equal to 0.11 J/mm was found to be martensitic metastable, whereas, for samples made with LED of 0.25 and 0.41 J/mm, the presence of a biphasic structure of $\alpha + \beta$ type was also found.

- The obtained corrosion results on the Flat AS mechanically polished samples show that the most influential factors on the corrosion resistance of the material are the degree of homogenization of the layers and the porosity distribution.

- In the mechanically polished 3D AS samples with 0.11 J/mm LED a homogeneous distribution of the layers favors an increase in corrosion resistance, while in the samples made with 0.25 J/mm LED the effect of the perimeter distribution of the porosity defects prevails, leading to low corrosion resistance values. This effect is greater than in the case of the flat samples because the complex geometry leads to a greater surface extension of the sample. In the samples with LED equal to 0.41 J/mm the formation of a predominantly metastable martensitic α' microstructure with small percentages of $\alpha + \beta$ biphasic microstructure contributes to the improvement of the material's corrosion resistance.

- For the 3D AS sample, the absence of mechanical polishing of the specimens reduces the negative effect produced by the mechanical treatment of removing the natural passivation layer of the AS specimens.

- Electrochemical characterizations suggest that the corrosion behavior of the Ti6Al4V samples produced by PBF-LB/M process is comparable with those reported in the literature for casting samples. Regardless of LED used during the PBF-LB/M process, AN samples have the lowest corrosion

current density, i.e., the longest working life, and the lowest passive current density, demonstrating the effectiveness of the anodizing process in producing a compact, uniform, and protective barrier-type anodic layer without flaws or heterogeneities on the surface of samples produced by PBF-LB/M.

Data availability

Data are fully available on request.

References

1. Pal S, Gubeljak N, Hudak R, Lojen G, Rajtukova V, Predan J, Kokol V, Drstvensek I (2019) Tensile properties of selective laser melting products affected by building orientation and energy density. Mater Sci Eng A 743:637–647. https://doi.org/10.1016/j.msea.2018.11.130

   Article **Google Scholar**

2. Gusarov AV, Grigoriev SN, Volosova MA, Melnik YA, Laskin A, Kotoban DV, Okunkova AA (2018) On productivity of laser additive manufacturing. J Mater Process Technol 261:213–232. https://doi.org/10.1016/j.jmatprotec.2018.05.033

   Article **Google Scholar**

3. Liu S, Shin YC (2019) Additive manufacturing of Ti6Al4V alloy: a review. Mater Des 164:107552. https://doi.org/10.1016/j.matdes.2018.107552

   Article **Google Scholar**

4. Shipley H, McDonnell D, Culleton M, Coull R, Lupoi R, O'Donnell G, Trimble D (2018) Optimisation of process parameters to address fundamental challenges during selective laser melting of Ti-6Al-4V: a review. Int J Mach Tools Manuf 128:1–20. https://doi.org/10.1016/j.ijmachtools.2018.01.003

   Article **Google Scholar**

5. Al-Mamun NS, MairajDeen K, Haider W, Asselin E, Shabib I (2020) Corrosion behavior and biocompatibility of additively manufactured 316L

stainless steel in a physiological environment: the effect of citrate ions. Addit Manuf 34:101237. https://doi.org/10.1016/j.addma.2020.101237

Article **Google Scholar**

6. Esmaily M, Zeng Z, Mortazavi AN, Gullino A, Choudhary S, Derra T, Benn F, D'Elia F, Müther M, Thomas S, Huang A, Allanore A, Kopp A, Birbilis N (2020) A detailed microstructural and corrosion analysis of magnesium alloy WE43 manufactured by selective laser melting, addit. Manuf 35:101321. https://doi.org/10.1016/j.addma.2020.101321

   Article **Google Scholar**

7. Metalnikov P, Ben-Hamu G, Eliezer D (2022) Corrosion behavior of AM-Ti-6Al-4V: a comparison between EBM and SLM. Prog Addit Manuf 7:509–520. https://doi.org/10.1007/s40964-022-00293-8

   Article **Google Scholar**

8. Mehta S, Jha S, Liang H (2022) Corrosion of nickel-based alloys fabricated through additive manufacturing: a review. Prog Addit Manuf. https://doi.org/10.1007/s40964-022-00298-3

   Article **Google Scholar**

9. Toptan F, Alves AC, Carvalho Ó, Bartolomeu F, Pinto AMP, Silva F, Miranda G (2019) Corrosion and tribocorrosion behaviour of Ti6Al4V produced by selective laser melting and hot pressing in comparison with the commercial alloy. J Mater Process Technol 266:239–245. https://doi.org/10.1016/j.jmatprotec.2018.11.008

   Article **Google Scholar**

10. Leon A, Levy GK, Ron T, Shirizly A, Aghion E (2020) The effect of hot isostatic pressure on the corrosion performance of Ti-6Al-4 V produced by an electron-beam melting additive manufacturing process. Addit Manuf 33:101039. https://doi.org/10.1016/j.addma.2020.101039

    Article **Google Scholar**

11. De Assis SL, Wolynec S, Costa I (2006) Corrosion characterization of titanium alloys by electrochemical techniques. Electrochim Acta 51:1815–1819. https://doi.org/10.1016/j.electacta.2005.02.121

Article **Google Scholar**

12. Qin T, Lin X, Yu J, Wang M, Guo P, Li J, Zhang Y, Liu J, Zhang S, Huang W (2021) Performance of different microstructure on electrochemical behaviors of laser solid formed Ti–6Al–4V alloy in NaCl solution. Corros Sci 185:109392. https://doi.org/10.1016/j.corsci.2021.109392

Article **Google Scholar**

13. Il Seo D, Lee JB (2020) Effects of competitive anion adsorption (Br− or Cl−) and semiconducting properties of the passive films on the corrosion behavior of the additively manufactured Ti–6Al–4V alloys. Corros Sci 173:108789. https://doi.org/10.1016/j.corsci.2020.108789

Article **Google Scholar**

14. Longhitano GA, Conde A, Arenas MA, Jardini AL, de Zavaglia CAC, MacielFilho R, de Damborenea JJ (2021) Corrosion resistance improvement of additive manufactured scaffolds by anodizing. Electrochim Acta 366:137423. https://doi.org/10.1016/j.electacta.2020.137423

Article **Google Scholar**

15. de Damborenea JJ, Larosa MA, Arenas MA, Hernández-López JM, Jardini AL, Ierardi MCF, Zavaglia CAC, Filho RM, Conde A (2015) Functionalization of Ti6Al4V scaffolds produced by direct metal laser for biomedical applications. Mater Des 83:6–13. https://doi.org/10.1016/j.matdes.2015.05.078

Article **Google Scholar**

16. Yin J, Peng G, Chen C, Yang J, Zhu H, Ke L, Wang Z, Wang D, Ma M, Wang G, Zeng X (2018) Thermal behavior and grain growth orientation during selective laser melting of Ti-6Al-4V alloy. J Mater Process Technol 260:57–65. https://doi.org/10.1016/j.jmatprotec.2018.04.035

Article **Google Scholar**

17. Dai N, Zhang LC, Zhang J, Chen Q, Wu M (2016) Corrosion behavior of selective laser melted Ti-6Al-4 V alloy in NaCl solution. Corros Sci 102:484–489. https://doi.org/10.1016/j.corsci.2015.10.041

Article **Google Scholar**

18. Dabrowski B, Swieszkowski W, Godlinski D, Kurzydlowski KJ (2010) Highly porous titanium scaffolds for orthopaedic applications. J Biomed Mater Res Part B Appl Biomater 95:53–61. https://doi.org/10.1002/jbm.b.31682

Article **Google Scholar**

19. Seah KHW, Thampuran R, Teoh SH (1998) The influence of pore morphology on corrosion. Corros Sci 40:547–556. https://doi.org/10.1016/S0010-938X(97)00152-2

Article **Google Scholar**

20. Xie FX, He XB, Cao SL, Lu X, Qu XH (2013) Structural characterization and electrochemical behavior of a laser-sintered porous Ti-10Mo alloy. Corros Sci 67:217–224

Article **Google Scholar**

21. Shi G, Guan C, Quan D, Wu D, Tang L, Gao T (2020) An aerospace bracket designed by thermo-elastic topology optimization and manufactured by additive manufacturing. Chin J Aeronaut 33:1252–1259. https://doi.org/10.1016/j.cja.2019.09.006

Article **Google Scholar**

22. Barriobero-Vila P, Gussone J, Haubrich J, Sandlöbes S, Da Silva JC, Cloetens P, Schell N, G. (2017) Requena, Inducing stable $\alpha + \beta$ microstructures during selective laser melting of Ti-6Al-4V using intensified intrinsic heat treatments. Materials (Basel). https://doi.org/10.3390/ma10030268

Article **Google Scholar**

23. Liu Y, Yang Y, Wang D (2016) A study on the residual stress during selective laser melting (SLM) of metallic powder. Int J Adv Manuf Technol 87:647–656. https://doi.org/10.1007/s00170-016-8466-y

Article **Google Scholar**

24. HemmasianEttefagh A, Zeng C, Guo S, Raush J (2019) Corrosion behavior of additively manufactured Ti-6Al-4V parts and the effect of post annealing, addit. Manuf 28:252–258. https://doi.org/10.1016/j.addma.2019.05.011

Article **Google Scholar**

25. Robinson JH, Ashton IRT, Jones E, Fox P, Sutcliffe C (2019) The effect of hatch angle rotation on parts manufactured using selective laser melting. Rapid Prototyp J 25:289–298. https://doi.org/10.1108/RPJ-06-2017-0111

Article **Google Scholar**

26. Ohmori Y, Nakai K, Ohtsubo H, Tsunofuri M (1994) Formation of widmastätten alpha structure in a Ti-6Al-4V alloy. Mater Transac JIM 35:238–246. https://doi.org/10.2320/matertrans1989.35.238

Article **Google Scholar**

27. Tamilselvi S, Murugaraj R, Rajendran N (2007) Electrochemical impedance spectroscopic studies of titanium and its alloys in saline medium. Mater Corros 58:113–120. https://doi.org/10.1002/maco.200603979

Article **Google Scholar**

28. Di Franco F, Zaffora A, Santamaria M, Di Quarto F (2018) Anodization and anodic oxides. In: Wandelt K (ed) Encyclopedia of interfacial chemistry: surface science and electrochemistry, vol 6. Elsevier, pp 26–40

Chapter **Google Scholar**

29. Tanvir MT, Fushimi K, Shimizu K, Nagata S, Skeldon P, Thompson GE, Habazaki H (2007) Influence of silicon on the growth of barrier-type anodic films on titanium. Electrochim Acta 52:6834–6840. https://doi.org/10.1016/j.electacta.2007.04.113

Article **Google Scholar**

30. Pourbaix M, Zhang H, Pourbaix A (1997) Presentation of an Atlas of chemical and electrochemical equilibria in the presence of a gaseous phase. Mater Sci Forum 251–254:143–148. https://doi.org/10.4028/www.scientific.net/msf.251-254.143

Article **Google Scholar**

31. Di Quarto F, Di Franco F, Monarca C, Santamaria M, Habazaki H (2013) Photoelectrochemical characterization of amorphous anodic films on Ti–

6at.%Si. Electrochim Acta 110:517–525. https://doi.org/10.1016/j.electacta.2013.01.120

Article **Google Scholar**

Download references

Funding

Regione Siciliana.